Available online at www.sciencedirect.com
SCIENCE DIRECT®
Geochimica et Cosmochimica Acta 70 (2006) 27–43
Geochimica
www.elsevier.com/locate/gca

Zinc sorption to biogenic hexagonal-birnessite particles within a hydrated bacterial biofilm

Brandy Toner [a,*], Alain Manceau [b], Samuel M. Webb [c], Garrison Sposito [a]

[a] Department of Environmental Science, Policy and Management, Division of Ecosystem Sciences, University of California, Berkeley, CA 94720-3114, USA
[b] Environmental Geochemistry Group, L.G.I.T.-Maison des Geosciences, Universite J. Fourier, B.P. 53, 38041 Grenoble Cedex 9, France
[c] Stanford Synchrotron Radiation Laboratory, Bldg. 137, MS 69, 2575 Sand Hill Rd., Menlo Park, CA 94025, USA

Received 14 February 2005; accepted in revised form 8 August 2005

Abstract

Biofilm-embedded Mn oxides exert important controls on trace metal cycling in aquatic and soil environments. The speciation and mobility of Zn in particular has been linked to Mn oxides found in streams, wetlands, soils, and aquifers. We investigated the mechanisms of Zn sorption to a biogenic Mn oxide within a biofilm produced by model soil and freshwater Mn^{II}-oxidizing bacteria *Pseudomonas putida*. The biogenic Mn oxide is a c-disordered birnessite with hexagonal layer symmetry. Zinc adsorption isotherm and Zn and Mn K-edge extended X-ray absorption fine structure (EXAFS) spectroscopy experiments were conducted at pH 6.9 to characterize Zn sorption to this biogenic Mn oxide, and to determine whether the bioorganic components of the biofilm affect metal sorption properties. The EXAFS data were analyzed by spectral fitting, principal component analysis, and linear least-squares fitting with reference spectra. Zinc speciation was found to change as Zn loading to the biosorbent [bacterial cells, extracellular polymeric substances (EPS), and biogenic Mn oxide] increased. At low Zn loading (0.13 ± 0.04 mol Zn kg^{-1} biosorbent), Zn was sorbed to crystallographically well-defined sites on the biogenic oxide layers in tetrahedral coordination to structural O atoms. The fit to the EXAFS spectrum was consistent with Zn sorption above and below the Mn^{IV} vacancy sites of the oxide layers. As Zn loading increased to 0.72 ± 0.04 mol Zn kg^{-1} biosorbent, Zn was also detected in octahedral coordination to these sites. Overall, our results indicate that the biofilm did not intervene in Zn sorption by the Mn-oxide because sorption to the organic material was observed only after all Mn vacancy sites were capped by Zn. The organic functional groups present in the biofilm contributed significantly to Zn removal from solution when Zn concentrations exceeded the sorption capacity of the biooxide. At the highest Zn loading studied, 1.50 ± 0.36 mol Zn kg^{-1} biosorbent, the proportion of total Zn sorption attributed to bioorganic material was 38 mol%. The maximum Zn loading to the biogenic oxide that we observed was 4.1 mol Zn kg^{-1} biogenic Mn oxide, corresponding to 0.37 ± 0.02 mol Zn mol^{-1} Mn. This loading is in excellent agreement with previous estimates of the content of cation vacancies in the biogenic oxide. The results of this study improve our knowledge of Zn speciation in natural systems and are consistent with those of Zn speciation in mineral soil fractions and ferromanganese nodules where the Mn oxides present are possibly biogenic.

1. Introduction

Microorganisms in soils, sediments, and natural waters influence the transport and fate of trace and contaminant metals through: (1) incorporation into biomass during growth, (2) metal complexation by cell/spore surfaces, extracellular polymers, and diffusible exudates (e.g., siderophores), (3) alteration of chemical microenvironment (e.g., O_2 and pH), (4) redox reactions with metal electron donors and acceptors, and (5) mineral formation and dissolution (Manceau and Combes, 1988; Bargar et al., 2000; Kraemer et al., 2002; Boyanov et al., 2003; Nelson and Lion, 2003; Wang et al., 2003; Kemner et al., 2004). The precipitation and subsequent surface reactivity of biogenic minerals is an expanding field of study, as these minerals are often small reactive particles that are spatially distributed as coatings at interfaces where biofilms form (Templeton

* Corresponding author.
E-mail address: btoner@whoi.edu (B. Toner).

0016-7037/$ - see front matter © 2005 Elsevier Inc. All rights reserved.
doi:10.1016/j.gca.2005.08.029

et al., 2001; Wilson et al., 2001; Chan et al., 2004). Biogenic and chemically precipitated (synthetic) Mn oxides are known to participate in a wide variety of redox and sorption reactions with metals and metalloids (Nelson and Lion, 2003; Tebo et al., 2004). Biofilm-embedded Mn oxides have been demonstrated to control Ni, Co, and Cr cycling in shallow seepage streams (Haack and Warren, 2003), and Pb sorption in Cayuga Lake, NY (Wilson et al., 2001). The speciation and mobility of Zn in particular is linked in part to Mn oxides in soils (Manceau et al., 2003), aquifers (Saunders et al., 1997), streams (Fuller and Harvey, 2000), and wetlands (Olivie-Lauquet et al., 2001).

Microbial biofilms possess metal complexing functional groups, which include carboxyl (–COOH), aldehyde (–COH), hydroxyl (–CHOH), sulfhydryl (–SH), phosphoryl ($–PO_4H_3$), and amine ($–NH_2$) groups (Sarret et al., 1998; Madigan et al., 2000; Kelly et al., 2002). The dominant functional groups controlling the Brønsted acidity of bacterial cell surfaces are carboxyl, phosphoryl, and hydroxyl/amine groups (Yee and Fein, 2001; Ngwenya et al., 2003). Of these functional groups, carboxyl and phosphoryl groups have been deemed particularly important in metal complexation (Sarret et al., 1998; Seki et al., 1998; Fein et al., 2001; Yee and Fein, 2001; Kelly et al., 2002; Ngwenya et al., 2003). For example, Zn sorption to *Bacillus subtilis* was best modeled as sorption to a combination of carboxyl and phosphoryl groups; Zn-carboxyl species were dominant at low pH, but the contribution of Zn-phosphoryl species increased as the pH approached circumneutral values (Fein et al., 2001). Ngwenya et al. (2003) measured Zn sorption to bacterial cells as a function of pH and found that a two-site model (Zn-phosphoryl and Zn-carboxyl species) greatly improved the fit to their experimental sorption data over a one-site model. Sarret et al. (1998) examined Zn sorption to fungal cell walls at pH 6 as a function of Zn loading. Zinc was predominantly associated with phosphoryl groups, and only at the highest Zn loading was a small (approximately 5% of Zn sorbed) association with carboxyl groups identified. Bacteria isolated from Zn contaminated lake sediments and grown in the presence of Zn exhibited Zn coordination to phosphate groups, likely at the cell outer membrane, and organic-sulfur groups, possibly thiol groups inside the cells (Webb et al., 2001).

Extended X-ray absorption fine structure (EXAFS) spectroscopy reveals the number of nearest neighbor atoms—for example, four oxygen atoms surrounding a Zn atom—and the distance between atoms, allowing the local bonding environment of the element of interest to be determined. This approach has been used extensively to examine Zn speciation in mineral/oxide suspensions (Silvester et al., 1997; Ford and Sparks, 2000; Manceau et al., 2002a; Waychunas et al., 2002; Li et al., 2004). In these latter studies, Zn coordination to first shell O falls into two categories, tetrahedral and octahedral. Zinc EXAFS spectra collected from samples containing tetrahedrally coordinated Zn exhibit four O atoms in the first shell of nearest neighbor atoms and an interatomic distance of approximately 1.97 Å (Sarret et al., 1998; Trainor et al., 2000). Zinc in octahedral coordination is identified by six O atoms in the first shell and interatomic distances of approximately 2.07–2.11 Å (Sarret et al., 1998; Waychunas et al., 2002).

Zinc sorption by a chemically synthesized birnessite (layer type Mn oxide with hexagonal symmetry; Silvester et al., 1997) was studied in detail with polarized EXAFS spectroscopy at pH 4 (Manceau et al., 2002a). This hexagonal birnessite has a negative structural charge arising from 16.7% Mn^{IV} vacancy and 11.1% Mn^{III} for Mn^{IV} substitution (Silvester et al., 1997). At low Zn loading, sorbed Zn was detected in tetrahedral coordination to O with a Zn–O interatomic distance of 1.97 Å (Manceau et al., 2002a). At high Zn loading, sorbed Zn was detected in combinations of tetrahedral and octahedral coordination (Manceau et al., 2002a). At both low and high Zn loadings, Zn shared three birnessite O atoms in a tridentate configuration at Mn vacancy sites. Zinc sorption to manganite (γ-MnOOH) as a function of pH was also studied by Zn EXAFS spectroscopy (Bochatay and Persson, 2000). In the first shell, the Zn–O interatomic distance changed from 2.04 to 1.96 Å as Zn loading increased, this shift was interpreted as a change from octahedral to tetrahedral coordination (Bochatay and Persson, 2000).

In the present study, the Mn oxide produced by *Pseudomonas putida* strain MnB1 was used as a model for Mn oxides formed in aquatic and soil environments. *P. putida* is a biofilm-forming bacteria that oxidizes Mn during the stationary phase of growth (Toner et al., 2005a). In the absence of Mn, the bacterial cells and associated extracellular polymeric substances (EPS) are effective Zn sorbing materials. (Toner et al., 2005b). Zinc sorption by the *P. putida* biofilm is attributed to approximately 20 mol% Zn-carboxyl and 80 mol% Zn-phosphoryl complexes, suggesting that at pH 6.9 the outer membrane of the Gram-negative cells is an important Zn-sorbing component of the biofilm (Toner et al., 2005b). The biogenic Mn oxide particles produced by this culture are precipitated immediately adjacent to the cell outer membranes and are embedded within hydrated EPS (Toner et al., 2005a). The biogenic Mn oxide, a birnessite, has an average Mn oxidation number of 3.90 ± 0.05, hexagonal layer symmetry, and a structural formula, as estimated from quantitative X-ray diffraction and Mn K-edge EXAFS spectroscopy, of $H_aNa_{0.15}(H_2O)_{0.45}Mn^{II,III}_{0.167}(H_2O)_{0.50}[Mn^{IV}_{0.833},vac_{0.167}]O_2$ (Villalobos et al., 2003; Villalobos et al., in press). In contrast to the hexagonal birnessite studied by Silvester et al. (1997) and Manceau et al. (2002a), this biogenic Mn oxide has a layer charge that originates only from vacant layer sites. However, the charge is balanced in both the synthetic and biogenic birnessite species by low-valent Mn cations (Mn^{II} and Mn^{III}) and by protons residing in the interlayer. An important similarity between the synthetic and biogenic birnessite species is the proportion of vacancy sites (16.7%).

The goal of this research was to characterize Zn sorption by a biogenic Mn oxide within a biofilm setting, and to determine whether the presence of bacterial cells and fully hydrated EPS (bioorganic material) affect the metal sorption properties of the Mn oxide. Zinc sorption experiments were conducted with *P. putida* in the presence of biogenic Mn oxide at pH 6.9. Zinc and Mn K-edge EXAFS spectroscopic data were collected for the Zn sorbed samples (EPS embedded cells and biogenic Mn oxide) under fully hydrated conditions. Spectral fitting, principal component analysis, and linear least-squares fitting of experimental EXAFS spectra were performed to interpret the data.

2. Methods

2.1. Sorption experiment

All solutions were prepared in MQ water (MilliPore Milli-Q, 18.2 MΩ cm) and sterilized by either filtration with 0.2 μm polyethersulfone (PES) membrane filters or autoclaving. *Pseudomonas putida* strain MnB1 was grown in liquid medium for seven days at 27 °C and 150 rpm, and in the presence of 1×10^{-3} M $MnCl_2$ (Villalobos et al., 2003). These growth conditions yielded a culture with approximately 0.3 g dry biosorbent and 0.07 g MnO_2 L^{-1} suspension. The culture contained large clusters of bacterial cells, along with biogenic Mn oxides, embedded in EPS (Toner et al., 2005a). The culture was cleaned of growth media by centrifuging (in sterile 250 mL PPCO bottles, 30 min, 10200 RCF) and resuspending the culture in pH 7, 0.01 M NaCl electrolyte solution three times. The pH of the resulting stock suspension was adjusted to pH 7.0 with additions 0.1 M NaOH and 0.1 M HCl and allowed to equilibrate overnight. The stock suspension was diluted gravimetrically 1:10. The resulting experimental suspension was weighed into batch reactors (sterile 250 mL Teflon bottles with Teflon coated stir bars). Additions of $ZnCl_2$ were made gravimetrically from a stock solution (pH 4.0, 0.01 M Zn, filter sterilized). Zinc sorption by biomaterial was measured at nine Zn concentrations, and the resulting samples are referred to as biomn1 through biomn9, lowest to highest Zn concentrations, respectively. The sorption experiment was conducted independently three times. Controls without solids, at low and high Zn concentrations, were prepared in Teflon bottles (no measurable Zn was sorbed by the containers). The batch reactors were placed on magnetic stirring platforms at room temperature (20 ± 2 °C). The pH of the sample suspensions was monitored at least four times daily during the experiment and maintained at 6.90 ± 0.15 by additions of 0.1 M NaOH or 0.1 M HCl. The pH probe required approximately 10 min to equilibrate with the suspension. The solution phase Zn concentration was measured 48 h after the pH stabilized. The samples for solution phase Zn concentration analysis were obtained by removing an aliquot of sample suspension while stirring the suspension vigorously. The aliquot was filtered, acidified, and analyzed by inductively coupled plasma-atomic emission spectrometry (ICP-AES, IRIS Thermo Jarrell Ash). Scandium was used as an internal instrument response standard. Calibration curves were constructed from gravimetrically prepared dilutions of plasma standards (VHG Labs, Manchester, NH). Linear regressions of instrument response versus calibration standard concentrations were prepared yielding calibration curves and 95% confidence intervals for calculated concentrations.

The concentration of biosorbent (g dry cells L^{-1}), in parallel experimental suspensions in the absence of Mn, was measured by collecting a sub-sample of the culture, rinsing the solid material to remove the NaCl, and drying the solid material from the suspension for greater than 24 h at 70 °C. The Mn oxide concentration (g MnO_2 L^{-1}) was measured by collecting a sub-sample of the experimental suspension and adding a sulfuric acid–oxalic acid solution to dissolve the Mn oxide solid (Freeman and Chapman, 1971), followed by ICP-AES analysis of total dissolved Mn. The final calculation of the biogenic Mn oxide concentration was based on the difference between the number of moles of Mn present in solution before and after dissolution. The conversion to units of g MnO_2 from molar concentration assumes the stoichiometry of the biogenic Mn oxide to be MnO_2.

The Zn removed from solution by the solid material of the sample suspensions (q, mol Zn kg^{-1} biomaterial) was quantified by the equation, $q = ([Zn]_0 - [Zn]_t)/[biosorbent]$, where $[Zn]_0$ and $[Zn]_t$ are the solution phase Zn concentrations at time zero and at the sampling time (mol Zn L^{-1}), and $[biosorbent]$ is the total mass (kg) of dry biomaterial in the sample suspension per liter. After examination of several alternative models, the Zn sorption data were modeled empirically with the van Bemmelen–Freundlich equation, $q = Ac^{\beta}$ where c is the equilibrium Zn concentration in mol Zn kg^{-1} suspension (Sposito, 2004). The adjustable parameters used to characterize the sorption isotherm data are A and β. Values of β vary between 0 and 1 (Sposito, 2004). The values of A and β were calculated by linearization of the van Bemmelen–Freundlich equation, $\log q = \log A + \beta \log c$, and are reported with 95% confidence intervals.

2.2. X-ray absorption spectroscopy

Zinc and Mn K-edge EXAFS spectra of reference materials and experimental samples were collected at beamlines 4-1 and 4-3 at Stanford Synchrotron Radiation Laboratory (SSRL). Zinc and Mn K-edge EXAFS spectra were collected using a Si(220) double crystal monochromator. The spectra for dilute samples were measured in fluorescence mode (using an Ar filled Lytle detector with a Cu filter), and those for concentrated samples in transmission mode. The monochromator energy for the Zn and Mn K-edge measurements was calibrated by using the adsorption edge of a Zn foil (9659 eV) and $KMnO_4$ (6543.34 eV), respectively.

The solid material of the Zn-sorbed samples was collected by centrifugation. The sample pastes were stored frozen until the time of analysis. The effect of sample freezing on Zn speciation was not examined. The sample material was packed into a PCTFE sample holder with Lexan windows and the sample holder was sealed with Kapton tape. The Lexan windows were used to prevent the Kapton tape adhesive from reacting with MnO_x species. The samples were kept moist and stored on ice until the EXAFS spectra were collected.

Zinc acetate, Zn phytate, Zn citrate, and Zn sorbed to δMnO_2 (Zn δMnO_2) reference materials were prepared. The organic reference materials were chosen to reflect the anticipated functional groups presented to solution by Gram-negative bacterial outer membranes (Fein et al., 2001; Kelly et al., 2001) and EPS, as well as those used for similar studies (Sarret et al., 1998). Zinc δMnO_2 was prepared as a reference material for Zn sorbed to a specimen Mn^{IV} oxide that has structural characteristics similar to the biogenic Mn oxide produced by *P. putida* (Villalobos et al., 2003). A summary of the conditions used to produce the reference materials is presented in Table 1. Unlike Zn acetate and Zn citrate, the stability constants for Zn phytate were not readily available. For Zn K-edge EXAFS spectra collection, Zn acetate, Zn phytate, and Zn citrate complexes were added to a PCTFE sample holder with Lexan windows as solutions, and the sample holder was sealed with Kapton tape. The δMnO_2 particles were collected by vacuum filtration, and the resulting wet paste was packed into a PCTFE sample holder with Lexan windows and sealed with Kapton tape. The Zn EXAFS spectrum of the Zn–Mn oxide chalcophanite was used as a reference in this study; the oxide has been characterized elsewhere (Manceau et al., 2002a).

The Zn and Mn EXAFS experimental and reference spectra were processed and analyzed using SixPack software (Webb, 2005) and a home-made software for data normalization and Fourier transformation (Villalobos et al., in press). The $\chi(k)$ spectra were k-weighted and Fourier transformed (FT) without smoothing in the k range of 3–12 $Å^{-1}$. The real and imaginary parts of the Zn FT$[\chi(k)k^3]$ were fit with phase and amplitude functions calculated with FEFF6 (Rehr et al., 1992) from the crystal structure of chalcophanite (Post and Appleman, 1988). The quality of each fit was evaluated quantitatively with the reduced chi square (χ^2_ν) and $\mathscr{R}$-factor parameters (Ravel, 2000). All fitted parameters [interatomic distance, R (Å), coordination number, N, and mean-square displacement of bond length, σ^2 ($Å^2$)] are presented with the estimated errors from IFEFFIT calculations (Newville, 2001). The error estimates reported by the IFEFFIT fitting routine are the diagonal elements of the covariance multiplied by $(\chi^2_\nu)^{1/2}$. The atom pairs used to model the Zn EXAFS spectra were linked such that a single value for the change in threshold energy, ΔE_0 (Teo and Joy, 1981), was obtained for each fit. In fits to both reference and experimental spectra the amplitude reduction factor (S_0^2) was set to 0.86, as determined by fitting of the EXAFS spectrum of chalcophanite.

Table 1
Summary of Zn EXAFS reference material preparation

	Zn acetate	Zn phytate	Zn citrate	Zn δMnO_2
Ligand (M)	2.0	Solubility limit[a]	2.0	0.09 g L^{-1}[b]
Zn (M)	0.5	<0.01	0.5	7.05×10^{-5}
pH	6	4	5	7
Complex1[c]	10% Zn[ace]	—	12% ZnH_2[cit]	—
Complex2	90% $Zn[ace]_2$	—	12% $Zn[cit]_2$	—
Complex3		—	76% Zn[cit]	—

Note. The δMnO_2 was provided by Dr. Villalobos (National University of Mexico), the synthesis recipe is published in Villalobos et al. (2003).

[a] Started with 0.1 M phytate, addition of $ZnCl_2$ caused precipitation of Zn phytate solid. The precipitate was removed by microfiltration and the final concentration was not measured.

[b] Solids concentration, Zn:Mn molar ratio 0.068.

[c] MINEQL+ results.

The Zn EXAFS data set was subjected to principal component analysis (PCA) to aid in determining the number and identity of the Zn species present in the Zn sorbed samples. The reader is referred to Manceau et al. (2002b) for a detailed treatment of the use of PCA in EXAFS spectroscopic analysis. The number of principal components represented by the data set was determined using the minimum of the indicator function (Malinowski, 1977). Target transformation analyses were conducted to evaluate the suitability of the Zn reference spectra for inclusion in the spectral data set using the SPOIL parameter (Malinowski, 1978). Values for SPOIL of less than 1.5 are considered excellent, 1.5–3 good, 3–4.5 fair, and 4.5–6 poor (Malinowski, 1978). The PCA was performed with unsmoothed, unfiltered k^3-weighted experimental spectra.

Using the component spectra identified by PCA, linear least-squares fitting of k-weighted experimental EXAFS spectra $[\chi(k)k^3]$ with the reference spectra was conducted. In the fits, the energy was not allowed to float and the component sum was not forced to equal 1.0. The numerical results of these linear fits are interpreted as the fractional contribution of each reference spectrum to the experimental spectrum, and therefore, are taken to indicate the proportion of each Zn species in the sample. In general, the precision of linear fitting is approximately ±10% (Manceau et al., 2000b; Isaure et al., 2002). However, it can be as low as approximately ±5% when (1) the spectrum from a species of interest has high amplitude or a distinctive feature, (2) the dataset is of high quality and well constrained (O'Day et al., 2004; Sarret et al., 2004; Bargar et al., 2005). The goodness of the linear fits was assessed by the minimization of the χ^2_ν parameter (Newville, 2001).

2.3. Synchrotron radiation X-ray diffraction

In-situ synchrotron-radiation X-ray diffraction (SR-XRD) patterns were collected at SSRL on beam line 2-1 using a Bicron photomultipler tube detector and a

Si(1 1 1) double crystal monochromator. The sample preparation and data collection are described in detail elsewhere (Bargar et al., 2005). The samples were analyzed as wet pastes of constant thickness in sealed transmission cells with Lexan windows. The wavelength used was 1.2410 ± 0.0001 Å, the focused beam dimensions were $\sim 1 \times 4$ mm, and the step size was 0.04° 2θ. The SR-XRD patterns were corrected for θ-dependent attenuation of incident and scattered X-rays. The SR-XRD patterns of the sample holder and water were subtracted from the sample patterns. To facilitate data interpretation, the observed XRD patterns were converted to Cu-Kα radiation (1.5418 Å wavelength) patterns and displayed as intensity versus ° 2θ.

3. Results

3.1. Zn sorption experiment

The Zn sorption isotherm is displayed in Fig. 1. The Zn loadings for each of the nine samples are displayed in Table 2. The biosorbent, consisting of bacterial cells and EPS (bioorganic material) plus biogenic Mn oxide, adsorbed 1.50 ± 0.36 mol Zn kg^{-1} biosorbent at the highest Zn loading (±2SD); this loading corresponds to 0.76 ± 0.13 mol Zn mol^{-1} Mn. The sorption data were fit with an empirical power law in the form of the van Bemmelen–Freundlich equation with parameters A and β having values of $16.0 \pm^{7.4}_{5.0}$ and 0.28 ± 0.03, respectively (±95% confidence interval). A single-site Langmuir model was not appropriate for the experimental data because a plot of the distribution coefficient (K_d, m^3 solution kg^{-1} sorbent) versus the loading (q, mol solute kg^{-1} sorbent) was nonlinear (Sposito, 2004). A two-term Langmuir model was then examined, but rejected because K_d did not appear to approach zero at a finite value of q (Sposito, 2004).

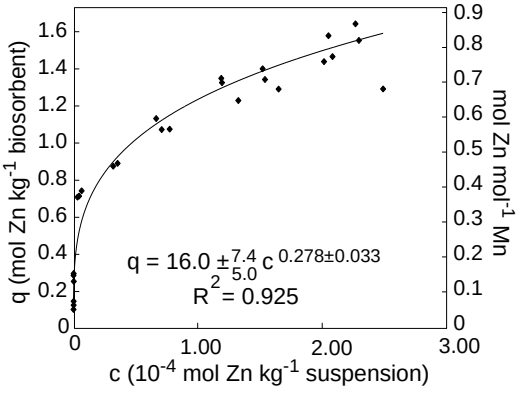

Fig. 1. Zinc sorption by biosorbent consisting of bacterial cell aggregates and associated biogenic Mn oxide embedded in EPS at pH 6.9 and 20 °C.

3.2. Zn EXAFS spectroscopy

Zinc K-edge EXAFS spectra were collected from all Zn sorbed samples listed in Table 2, except biomn2 and biomn8. Spectra collected for samples biomn1, biomn3, and Zn δMnO_2 are presented and compared to that of chalcophanite in Fig. 2. The two spectra from biogenic samples are right shifted relative to that of chalcophanite, indicating shorter average interatomic distances; this shift is Zn loading-dependent and is greater for the spectra collected from sample biomn1 than biomn3 (Figs. 2A and B). A similar spectral evolution with Zn loading has been observed previously in spectra collected for Zn sorbed birnessite samples, and was shown to arise from a change from tetrahedral coordination to a combination of tetrahedral and octahedral coordination (Manceau et al., 2002a). The spectrum collected from chalcophanite is shifted to lower k-values relative to that of Zn δMnO_2; however, the phase of the spectrum from Zn δMnO_2 is more similar to that of chalcophanite than either biomn1 or biomn3 (Fig. 2C).

The Fourier transforms (FTs) of spectra from samples biomn1, biomn3, and reference material Zn δMnO_2 are presented and compared to that of chalcophanite in Fig. 3. The structure of chalcophanite has been described previously by XRD (Post and Appleman, 1988) and EXAFS spectroscopy (Manceau et al., 2002a). The most intense FT peaks derived from the chalcophanite EXAFS data are produced by Zn–O1 in the first shell, Zn–Mn1 in the second shell, and Zn–Mn2 in the third shell (Fig. 3A); biomn1, biomn3, and Zn δMnO_2 share this general three-peak character. As suggested by the EXAFS spectra, the average first shell interatomic distances in the chalcophanite structure are greater than those of biomn1,

Table 2
Summary of sample names and Zn loadings

Sample	Replicates (mol Zn (kg biosorbent)$^{-1}$)			Average (mol Zn (kg biosorbent)$^{-1}$)	2SD (mol Zn (kg biosorbent)$^{-1}$)	EXAFS collected
biomn1	0.15	0.10	0.13	0.13	0.04	y
biomn2	0.30	0.29	0.25	0.28	0.04	n
biomn3	0.74	0.71	0.71	0.72	0.04	y
biomn4	0.89	0.88	—	0.88	0.02	y
biomn5	1.08	1.07	1.13	1.07	0.06	y
biomn6	1.23	1.33	1.35	1.30	0.13	y
biomn7	1.29	1.40	1.34	1.34	0.11	y
biomn8	1.44	1.58	1.47	1.49	0.15	n
biomn9	1.29	1.64	1.55	1.50	0.36	y

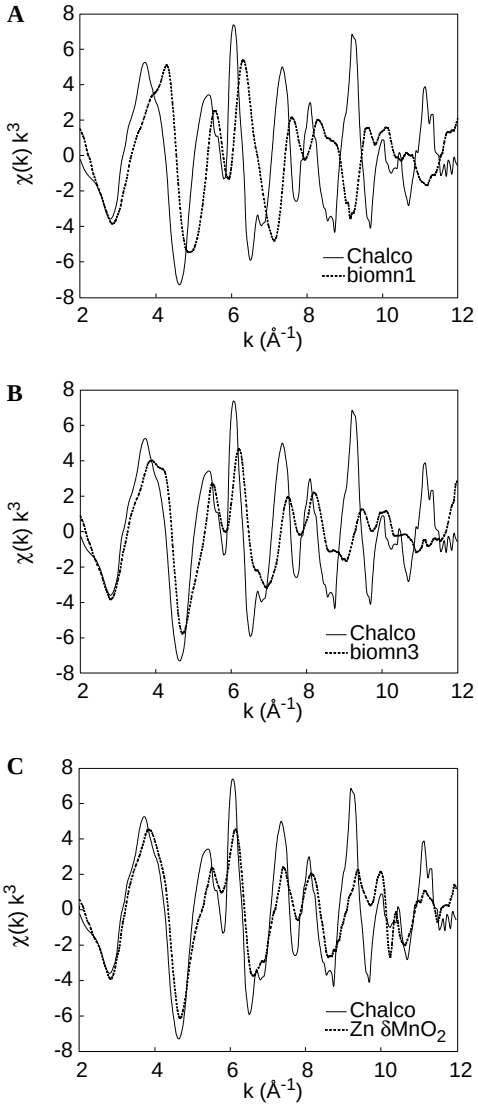

Fig. 2. Comparison of Zn EXAFS data collected for samples biomn1 and biomn3 and reference Zn δMnO_2 to that of chalcophanite. At low Zn loading to biosorbent (bacterial cell aggregates and associated biogenic Mn oxide embedded in EPS) (A) the spectra are out of phase. As Zn loading to the biosorbent increases (B), the sample spectrum shifts toward the chalcophanite spectrum at lower k values. (C) Zinc sorbed to the synthetic Mn oxide δMnO_2 is more in phase with chalcophanite than are the biogenic samples, but differs in amplitude and shape particularly at higher k values.

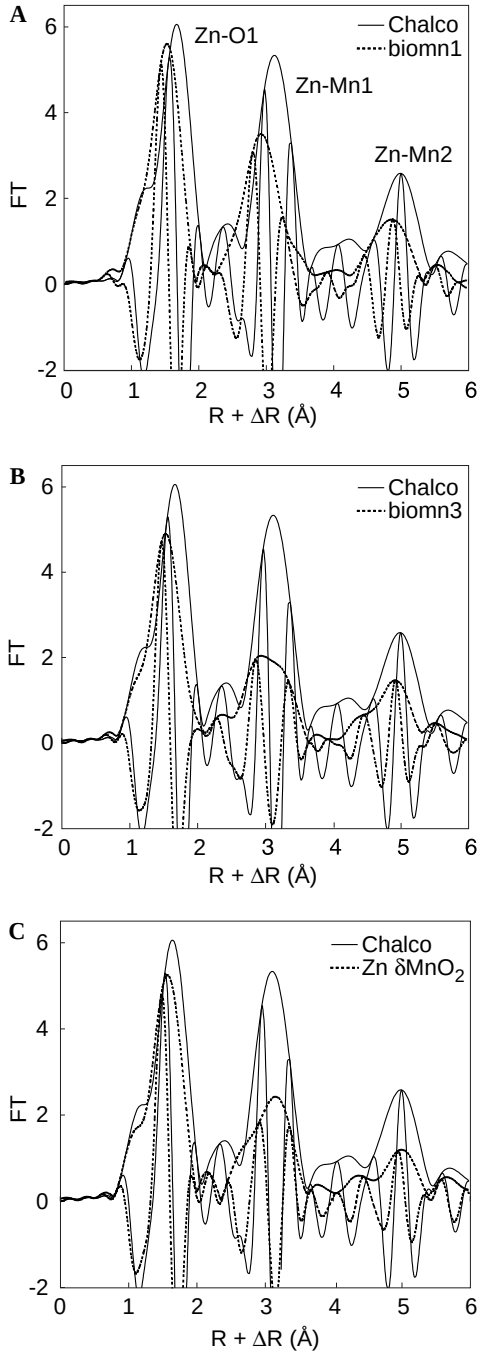

Fig. 3. Comparison of Fourier transforms of Zn EXAFS data collected for samples biomn1 and biomn3 and reference Zn δMnO_2 to that of chalcophanite. (A) The chalcophanite structure produces three peaks, first shell Zn–O1, second shell Zn–Mn1, and third shell Zn–Mn2. The first shell peak in data from sample biomn1 (A), sample biomn3 (B), and reference Zn δMnO_2 (C) are shifted to shorter average interatomic distances relative to chalcophanite. The second Zn–Mn1 peak in the data for sample biomn3 and reference Zn δMnO_2 exhibit peak asymmetry and marked decrease in amplitude.

biomn3, and Zn δMnO_2, with Zn δMnO_2 most closely resembling the average interatomic spacing in the chalcophanite structure (Fig. 3C). Relative to the data collected for sample biomn1 and reference material chalcophanite, the second shell of biomn3 and Zn δMnO_2 exhibit peak asymmetry and reduction in amplitude, perhaps indicating the presence of overlapping subshells.

Chalcophanite, $ZnMn_3O_7 \cdot 3H_2O$, is a Zn–Mn oxide with a layer-type structure. It is composed of layers of edge-sharing Mn^{IV}–O octahedra with one in seven octahedral vacancies (Post and Appleman, 1988). These structural Mn vacancies are capped above and below by Zn^{II} in octahedral coordination to three O atoms of the Mn vacancy and three O atoms through waters of hydration (Fig. 4). The chalcophanite structure, as provided by XRD analysis, has two Zn–Mn1 subshells—3 Mn atoms at 3.486 Å and 3 Mn atoms at 3.498 Å (Post and Appleman, 1988). These

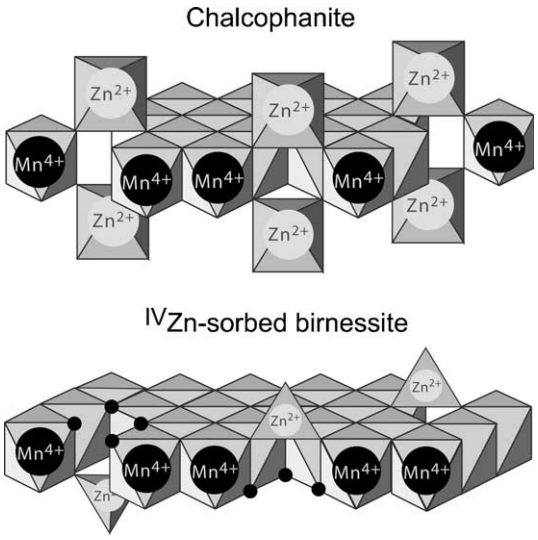

Fig. 4. Polyhedral representation of a single layer of chalcophanite (top) and Zn tetrahedrally coordinated (^{IV}Zn) to vacancy sites of hexagonal birnessite.

two subshells are not resolved by EXAFS spectroscopy. Therefore, the second shell Zn–Mn1 contribution to the FT data collected for chalcophanite was simulated with 6.0 ± 1.2 Mn atoms at a distance of 3.52 ± 0.02 Å; the simulation reproduces well the wave envelope, phase, and amplitude of the data (Fig. 5A).

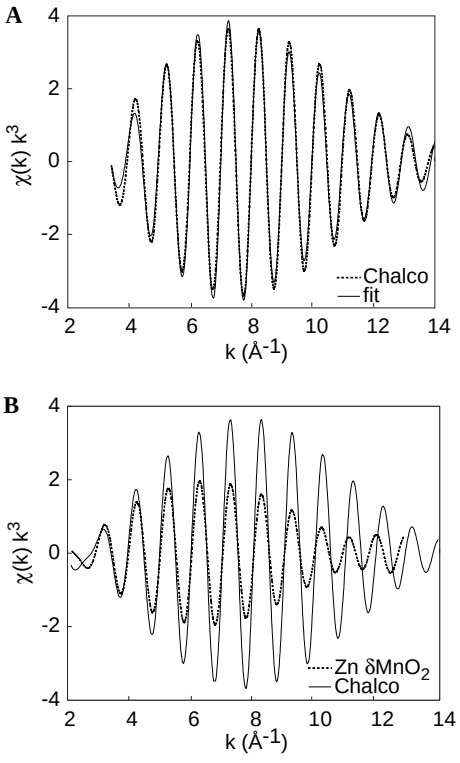

Fig. 5. The second shell of chalcophanite, Zn–Mn1 (see Fig. 3A), is simulated at $R = 3.52$ Å, $N = 6.0$, $\sigma^2 = 0.007$ Å^2, and $S_0^2 = 0.86$ (A). A comparison of the reverse FTs of the second shell Mn contribution for chalcophanite and Zn δMnO_2 data is displayed (B). The reverse FT ranges for the data were 2.7–3.6 and 2.4–3.6 $R + \Delta R$ (Å), respectively.

The reverse FT of the second shell Zn–Mn1 contribution to the data collected for chalcophanite and Zn δMnO_2 are compared in Fig. 5B. The two waves have a similar envelope, suggesting that they arise from the same atomic pair. However, the Zn δMnO_2 wave is damped, likely due to greater structural disorder in the Zn δMnO_2 than in chalcophanite. In addition, the waves are out of phase at high k values, possibly from a split Zn–Mn1 shell in the data collected for Zn δMnO_2. To test this hypothesis we simulated the second shell of the Zn δMnO_2 data with one Zn–Mn1 shell, and then with two Zn–Mn1 subshells (Fig. 6). A single Zn–Mn1 shell at 3.53 ± 0.02 Å ($N = 6.1 \pm 1.2$, $\sigma^2 = 0.013$ Å^2) did reproduce the wave envelope, but was not able to replicate the high k phase and amplitude of the wave (Fig. 6A). Two Zn–Mn1 subshells, at 3.39 ± 0.02 Å ($N = 1.8 \pm 0.4$) and 3.53 ± 0.02 Å ($N = 4.0 \pm 0.8$), better reproduced the wave phase and amplitude at high k (Fig. 6B, Table 3). The presence of two Zn–Mn1 subshells suggests that the Zn sorbed δMnO_2 reference material has both tetrahedrally and octahedrally coordinated Zn species (Manceau et al., 2002a). The fitting results for the first-shell Zn δMnO_2 data are reported in Table 3, d(Zn–O1) $= 2.07 \pm 0.02$ Å, $N = 5.7 \pm 1.1$, and $\sigma^2 = 0.011$. Despite the clear second-shell evidence for

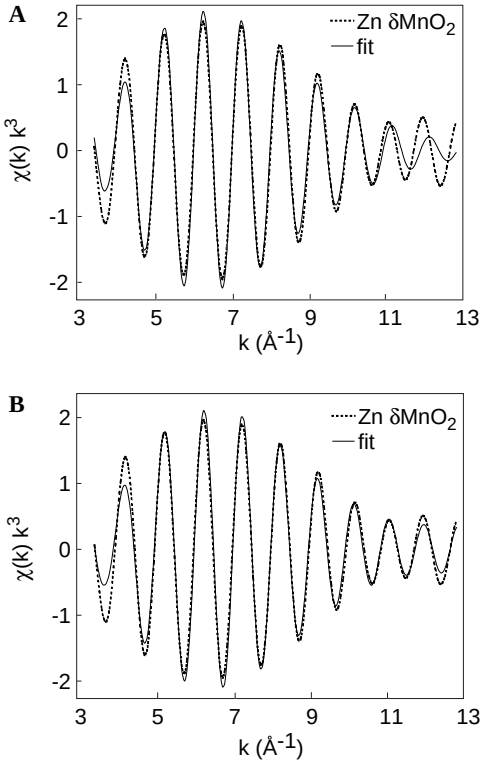

Fig. 6. Simulation of the second shell Zn–Mn1 contribution to Zn sorbed δMnO_2 data with one Mn shell at an interatomic distance of $R = 3.53$ Å, $N = 6.1$, $\sigma^2 = 0.013$ Å^2, and $S_0^2 = 0.86$ (A), and two Mn subshells at interatomic distances of $R = 3.39$ Å, $N = 1.8$, and $\sigma^2 = 0.008$ Å^2, and $R = 3.53$ Å, $N = 4.0$, $\sigma^2 = 0.008$ Å^2, and $S_0^2 = 0.86$ (B). The reverse FT range for the data was 2.4–3.6$R + \Delta R$ (Å). The two subshell fit better reproduces the high k features of the wave.

Table 3
Comparison of structural parameters for Zn in chalcophanite, octahedrally/tetrahedrally coordinated Zn-birnessite, Zn δMnO_2, tetrahedrally coordinated Zn-birnessite, sample biomn1, and sample biomn3

Atom pair	Chalcophanite		$^{IV/VI}$Zn-birn		Zn δMnO_2		^{IV}Zn-birn		biomn1		biomn3	
	R (Å)[a]	N[b]	R (Å)	N	R (Å)	N	R (Å)	N	R (Å)	N	R (Å)	N
Zn–O1	2.07	3	2.02	2.6	2.07 (0.02)	5.7 (1.1)	1.97	3.3	1.97 (0.01)	4.4 (0.7)	1.97[c]	1.9 (1.1)
Zn–O2	2.14	3	2.15	2.6	—	—	—	—	—	—	2.11 (0.03)	3.5 (1.5)
Zn–Mn1	3.49	3	3.48	6.1	3.39 (0.02)	1.8 (0.4)	3.35	2.9	3.36 (0.03)	5.7 (1.0)	3.35 (0.03)	1.9[d]
	3.50	3	—	—	3.53 (0.02)	4.0 (0.8)	3.50	2.0	—	—	3.51 (0.02)	3.5[e]
Zn–Mn_{adj}	5.14	3	5.16	3.0	—	—	—	—	—	—	—	—
Zn–Mn2	5.38	6	5.38	6.0	—	—	—	—	—	—	—	—

Chalcophanite values are from XRD (Post and Appleman, 1988). $^{IV/VI}$Zn-birn and ^{IV}Zn-birn are EXAFS fits for Zn sorbed birnessite in octahedral/tetrahedral (sample ZnBi128) and tetrahedral coordination (sample ZnBi8), respectively (Manceau et al., 2002a). EXAFS fit parameters for Zn δMnO_2, biomn1, and biomn3 are from this work, $S_0^2 = 0.86$. The σ^2 (Å^2) values from top to bottom in each column are (1) Zn δMnO_2 0.011 (0.002), 0.008 (0.005), 0.008 (0.005), (2) biomn1 0.007 (0.001), and 0.012 (set), and (3) biomn3 0.003 (0.001), 0.008 (0.006), 0.006 (0.002), 0.008 (0.004). The symbol "—" indicates that either the value was not reported or is not applicable.

[a] Distance between the atoms in the atom pair.
[b] Number of neighboring atoms.
[c] Constant in final fit.
[d] Set equal to N(Zn–O1).
[e] Set equal to N(Zn–O2).

two Zn-sorbed species, the first-shell simulation of the δMnO_2 data was not improved by the addition of a second Zn–O pair. We propose that the Zn–O1 interatomic distance, 2.07 ± 0.02 Å, is a weighted average between tetrahedral and octahedral Zn sorbed species, e.g., first shell Zn–O interatomic distances of 2.02 Å (tetrahedral + octahedral) and 2.15 Å (octahedral) were observed in Zn sorbed birnessite (Table 3; Manceau et al., 2002a). The relatively large σ^2 value also suggests more than one Zn–O pair is present in the first shell.

A fit to the spectrum from sample biomn1, the lowest Zn loading, is displayed in Fig. 7. The fitting parameters for the data are summarized in Table 3. A two-shell fit to the data from biomn1 accounted for the first two major FT peaks in the R range of 1–6 (Å), Zn–O1 and Zn–Mn1 (Fig. 7A). In the first shell, 4.4 ± 0.7 O atoms were fit at 1.97 ± 0.01 Å. In the second shell, 5.7 ± 1.0 Mn atoms were fit at 3.36 ± 0.03 Å. The position of the third FT peak (5.36 Å), presumably Zn–Mn2, is consistent with that reported by Manceau et al. (2002a); however, large error estimates for parameters N and σ^2 prevented a reliable fit for the third shell peak. The coordination numbers and interatomic distances provided by the fit suggest that at the lowest Zn loading examined there was only one Zn species present, Zn sorbed in tetrahedral coordination to the biogenic Mn oxide.

The result of a linear least-squares fit to the Zn δMnO_2 spectrum with component spectra from sample biomn1 (tetrahedral coordination) and reference material chalcophanite (octahedral coordination) is presented in Fig. 8A. The fit indicates that Zn speciation in the Zn sorbed δMnO_2 reference can be modeled by 42 ± 5 mol% tetrahedrally coordinated Zn and 58 ± 5 mol% octahedrally coordinated Zn. The coordination numbers (N, Table 3) from the spectral fit to Zn δMnO_2 data can also be used to estimate the propor-

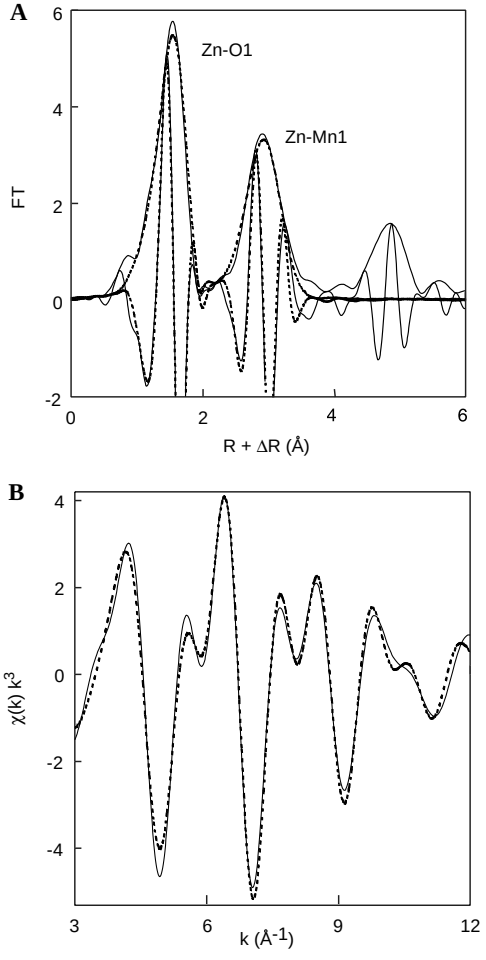

Fig. 7. Results of a two shell fit to the Zn EXAFS data collected for sample biomn1 displayed in (A) real space and (B) k-space. The reverse FT range was 1–3.5R + ΔR (Å). The biomn1 data are the solid lines, the simulations are the dashed lines. The fit parameters are reported in Table 3.

tion of tetrahedral and octahedral Zn species: 28 ± 7 mol% tetrahedral ($1.8 \pm 0.4/6 = 0.28 \pm 0.07$) and 67 ± 13 mol % octahedral ($4.0 \pm 0.8/6 = 0.67 \pm 0.13$) Zn-sorbed species. In this two-component system, shell-by-shell and linear least-squares fitting results are indistinguishable for the octahedrally coordinated Zn species and agree within a 2 mol% for the tetrahedrally coordinated species.

As for the reference material Zn δMnO_2, the data collected for sample biomn3 were fit with tetrahedral and octahedral subshells for each of the Zn–O1 and Zn–Mn1 peaks—the fit parameters are displayed in Table 3. However, attempts to obtain shell-by-shell fits to the spectra collected for samples biomn4, biomn5, biomn6, biomn7, and biomn9, using the parameters obtained from the fits to spectra from biomn1, biomn3, Zn δMnO_2, and chalcophanite, were unsatisfying due to the large number of atomic pairs produced by the combination of the tetrahedral and octahedral Zn species and possibly to additional/other unknown components (e.g., Zn organic species). Therefore, principal component analysis (PCA) was performed with all of the experimental Zn K-edge EXAFS data. The minimum of the indicator function was located at three spectral components, and the spectral components are displayed in Fig. 9A. Target transformation analyses were conducted with reference spectra from Zn δMnO_2, chalcophanite, Zn phytate, Zn acetate, and Zn citrate. The spectral results of these target transformation analyses are displayed in Figs. 9B–F. The SPOIL values for reference spectra from Zn δMnO_2, chalcophanite, Zn phytate, Zn acetate, and Zn citrate are 2.3, 3.2, 2.5, 2.6, and 4.2, respectively. Therefore, the reference spectra from Zn δMnO_2, Zn phytate, and Zn acetate are considered good representatives, and the reference spectra from chalcophanite and Zn citrate fair representatives for the Zn sorbed data. A spectrum collected from aqueous $ZnNO_3$ had a SPOIL value of 6.3 (data not shown) and is considered a poor representative for the Zn sorbed data.

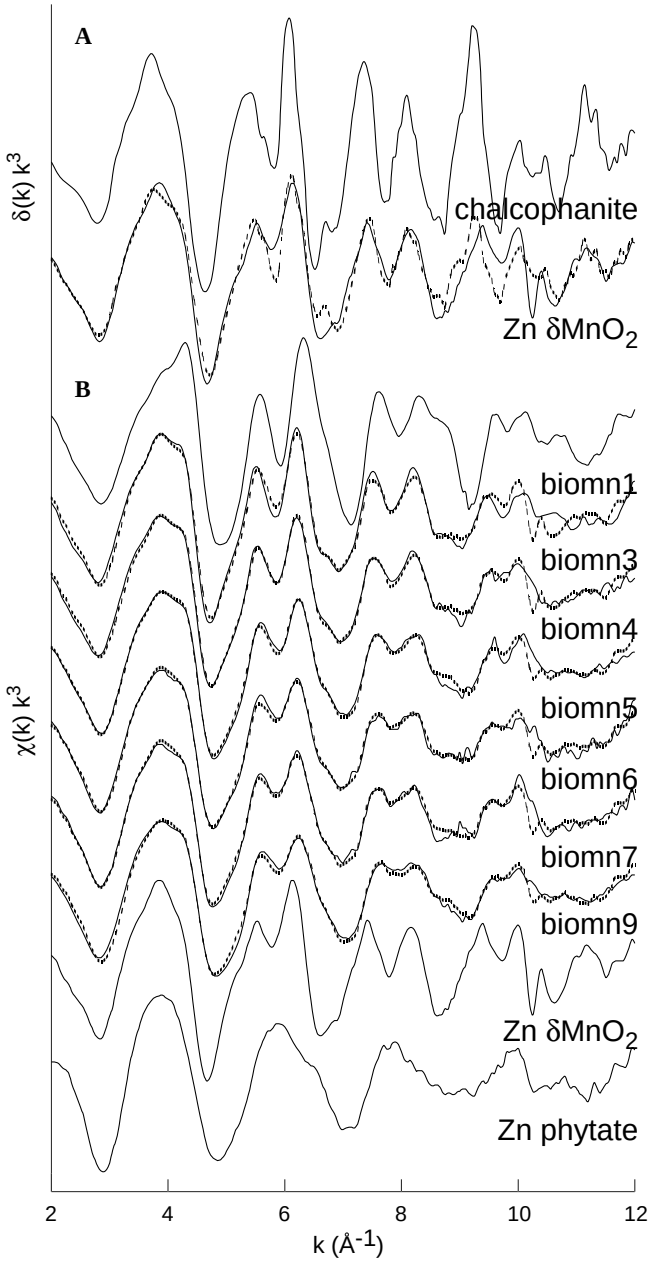

Fig. 8. (A) Linear least-squares fit to Zn EXAFS spectrum collected for reference Zn δMnO_2. The component spectra are tetrahedrally coordinated biomn1 and octahedrally coordinated chalcophanite. (B) Linear least-squares fits to experimental Zn EXAFS spectra. The component spectra from biomn1, Zn δMnO_2, and Zn phytate are displayed. The sample and component spectra are solid lines, the linear fits to the data are dashed lines. The results of the fits are reported in Table 4.

Two- and three-component linear least-squares fits to the EXAFS spectra were conducted with the experimental spectrum from biomn1 (as an end-member component, see Discussion), reference spectrum from Zn δMnO_2, and reference spectra from Zn phytate or Zn acetate (Fig. 8B). The spectra from sample biomn1 and reference material Zn δMnO_2 represent Zn sorbed to Mn oxide in tetrahedral and a combination of tetrahedral and octahedral coordination, respectively. The spectra collected from the Zn phytate and Zn acetate reference materials represent the spectral signature of Zn-complexes with organic functional groups present in the bioorganic portion of the samples. The numerical results of these fits using either spectra from Zn phytate or Zn acetate are listed in Table 4. The spectrum collected from sample biomn3 was best fit with two components, biomn1 and Zn δMnO_2. Therefore, in agreement with the shell-by-shell fitting results, we conclude that all of the spectroscopically detectable Zn was sorbed to biogenic Mn oxide at this Zn loading. The spectra collected from samples biomn4, biomn5, biomn6, biomn7, and biomn9 were best fit with three components, biomn1, Zn δMnO_2, and either Zn phytate or Zn acetate. The spectra from Zn phytate and Zn acetate were equally good representatives for the data. In the three component fits to the experimental spectra, the contribution of Zn phytate or Zn acetate spectra increased as Zn loading to the sample increased. This result indicates that the bioorganic material begins to contribute to Zn sorp-

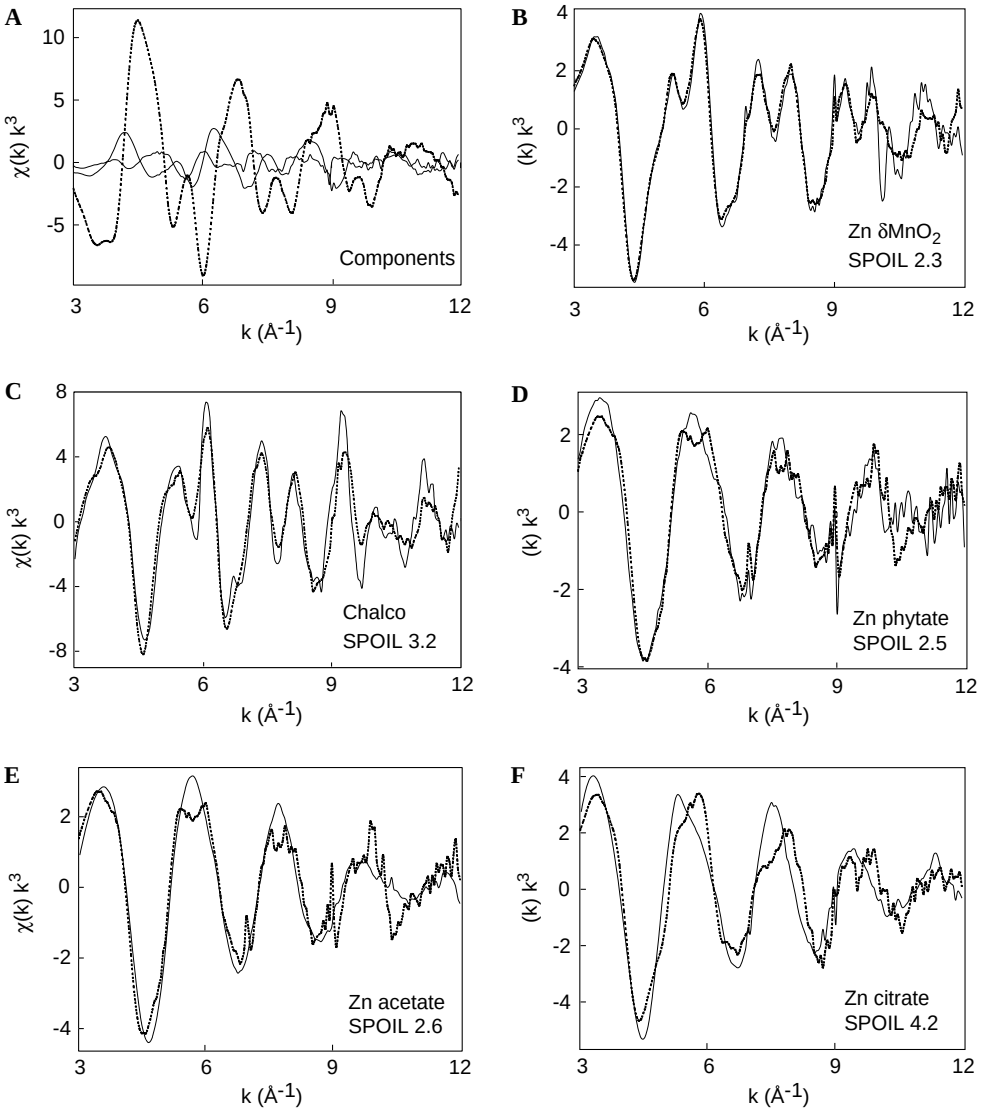

Fig. 9. The three principal components (A) of the Zn EXAFS k^3-weighted data set, and the target transformation analysis results for the proposed reference spectra Zn δMnO_2 and chalcophanite (B–C), and aqueous complexes of Zn phytate, Zn acetate, and Zn citrate (D–F). The reference spectra are solid lines, the target transform results are the dashed lines.

tion above loadings of 0.37 mol Zn mol^{-1} Mn (sample biomn3), and is responsible for essentially all Zn sorption in samples above this loading (Table 4). Although the 5 mol% contribution of the Zn-organic species to spectrum biomn4 is at or below the usual detection limit reported for linear least-squares fitting of EXAFS data (ca. 10 mol%), the addition of the third Zn-organic component to the linear fit improved the χ_v^2 by 7%. Adding the third Zn-organic component to the linear fit to spectrum biomn5 improved the χ_v^2 by 70%. Therefore, for this data set we use an error estimate for the linear least-squares fit values of ±5 mol%.

3.3. Mn EXAFS spectroscopy

Manganese K-edge EXAFS spectra were collected for biogenic Mn oxide with and without sorbed Zn. The spectra for samples biomn1 and biomn9 are displayed in Fig. 10A. The EXAFS spectra from the biogenic Mn oxide and sample biomn1 were identical; therefore, Zn sorption at the lowest loading did not change the Mn local structure within the detection limit of EXAFS (biogenic Mn oxide spectrum not shown). However, as Zn loading increased spectral changes were observed indicating that Mn speciation within the sample had changed. Of particular interest was the disappearance of the shoulder at 6.5 $Å^{-1}$ as Zn loading increased (Fig. 10A, arrow). The spectral changes in the Mn EXAFS spectrum of biomn9 are also visible in the FT[$\chi(k)k$] (Fig. 10B). In contrast to the increase in amplitude of the first and second shell Mn–O1 and Mn–Mn1 peaks, the small third shell peak observed at 3.10 Å for biomn1 data decreased as Zn loading increased (Fig. 10B, inset). These structural changes suggest that the decrease in peak at 3.10 Å was not caused by increased structural disorder of Mn speciation as loading increased. The biomn9 data are also compared to the data collected

Table 4
Linear least-squares fitting results for Zn EXAFS $\chi(k)k^3$ spectra, and summary of Zn loading to biooxide and bioorganic components of the biofilm

Sample	χ_v^2	Comp. sum	Fit components			Loading (mol Zn/kg biosorbent)		
			biomn1	Zn δMnO_2	Zn phytate	Biooxide	Bioorganic	Total
biomn3	0.07	1.05	0.41	0.64	—	0.8	0.0	0.72
biomn4	0.03	0.98	0.41	0.51	0.05	0.8	0.0	0.88
biomn5	0.03	0.95	0.36	0.40	0.18	0.8	0.2	1.07
biomn6	0.05	0.97	0.31	0.35	0.31	0.9	0.4	1.30
biomn7	0.02	0.94	0.27	0.38	0.29	0.9	0.4	1.34
biomn9	0.03	0.91	0.32	0.20	0.38	0.8	0.6	1.50
			biomn1	Zn δMnO_2	Zn acetate			
biomn3	0.07	1.05	0.41	0.64	—	0.8	0.0	0.72
biomn4	0.03	0.98	0.41	0.52	0.05	0.8	0.0	0.88
biomn5	0.03	0.93	0.37	0.40	0.16	0.8	0.2	1.07
biomn6	0.06	0.94	0.33	0.36	0.25	0.9	0.3	1.30
biomn7	0.02	0.92	0.32	0.31	0.29	0.8	0.4	1.34
biomn9	0.03	0.88	0.35	0.15	0.38	0.7	0.6	1.50

Note. The error estimate for the linear least-squares fits is ±0.05. The Total loading to biosorbent data is adsorption isotherm data from Table 2. Zinc loading to Biooxide and Bioorganic components of the samples is calculated by multiplying the linear fit fractional component with the total sorbed Zn. The Biooxide loading includes tetrahedrally and octahedrally coordinated Zn species. The Bioorganic loading is calculated with the Zn phytate or Zn acetate component and represents Zn sorption by the organic functional groups present in the cells and EPS.

for the synthetic Mn oxides, δMnO_2 and acid birnessite (Figs. 10C–F). Acid birnessite and δMnO_2 are chemically synthesized layer type Mn oxides with structural characteristics similar to those of the biogenic Mn oxide (Villalobos et al., 2003). Selected physical and chemical properties for these two references and the biogenic Mn oxide are presented in Table 5. The amplitude of the third peak in the FT[$\chi(k)k$] of biomn9 data is slightly larger than that of δMnO_2 (Fig. 10D and inset) and close to that of acid birnessite (Fig. 10F and inset).

3.4. Synchrotron radiation X-ray diffraction

The fully hydrated biogenic Mn oxide (in the presence of cells and EPS, and aged 7 days) exhibited diffraction peaks at 1.23, 1.42, 2.45, ~4 and ~9 Å (Fig. 11). Apart from the basal 0 0 1 reflection at 9 Å, and the 4 Å peak which is obscured by a broad feature in the organic fraction, the pattern is in agreement with that reported for the air-dry specimen of the same biogenic oxide (Villalobos et al., in press). The expansion from ~7.6 to ~9 Å of the 0 0 1 reflection in the hydrated state is due to the insertion of a second layer of water molecules in the interlayer space.

4. Discussion

The Langmuir adsorption isotherm equation is often used to model metal sorption data (see cited literature below). The q_{max} parameter of the Langmuir model represents the metal loading that is approached asymptotically as the equilibrium metal concentration becomes very large (Sposito, 2004). The Langmuir equation was not used to model the data in the present study (see Results section); however, the results of previous studies of Zn sorption by microorganisms and Mn oxides in which the Langmuir model was applicable are discussed to provide context for the Zn loading values obtained in this study.

The range of values of Zn loading to the biogenic Mn oxide plus bioorganic material was 0.13–1.50 mol Zn kg^{-1} biosorbent; the range of initial Zn concentrations for the samples was 6.0–300.0 μM Zn. For comparison, the value of q_{max} for Zn adsorption by *Penicillium chrysogenum*, a filamentous fungi, is 0.2 mol Zn kg^{-1} dry cell material at pH 6 (Sarret et al., 1998). At pH 7, the Gram-positive bacteria *Bacillus subtilis* sorbed 0.1 mol Zn kg^{-1} of dry cell material (Fein et al., 2001).

In sample biomn3, Zn was associated only with oxide surfaces, and therefore, the maximum Zn loading to the biogenic Mn oxide observed in this study was 4.1 mol Zn kg^{-1} MnO_2. For comparison, the maximum Zn loading to a synthetic birnessite and δMnO_2 at pH 7 (calculated from published data) is 1.6 mol Zn kg^{-1} birnessite (McKenzie, 1980) and 1.2 mol Zn kg^{-1} δMnO_2 (Catts and Langmuir, 1986), respectively. The largest observed Zn loading to the biogenic Mn oxide produced by *P. putida*, in this study, is in general agreement with the value of q_{max} reported for Pb^{+2} sorption to fresh synthetic Mn oxide (2.5 mol Pb kg^{-1} Mn oxide), and for biogenic Mn oxide (6.3 mol Pb kg^{-1} Mn oxide) produced by *Leptothrix discophora* (Nelson and Lion, 2003). Li et al. (2004) used an empirical power law relationship to model the adsorption of Zn to a synthetic δMnO_2 at pH 5.5, yielding fit parameters $A = 18.74$ and $\beta = 0.287$. These A and β values are statistically indistinguishable from those reported here ($A = 16.0 \pm^{7.4}_{5.0}$, $\beta = 0.28 \pm 0.03$) despite the presence of bioorganic material (bacterial cells and EPS) in our samples.

The local structure of Zn sorbed to biogenic Mn oxide at the lowest loading (sample biomn1, Zn:Mn molar ratio 0.06) was interpreted as Zn in tetrahedral coordination to O atoms. This conclusion is based on the number of nearest

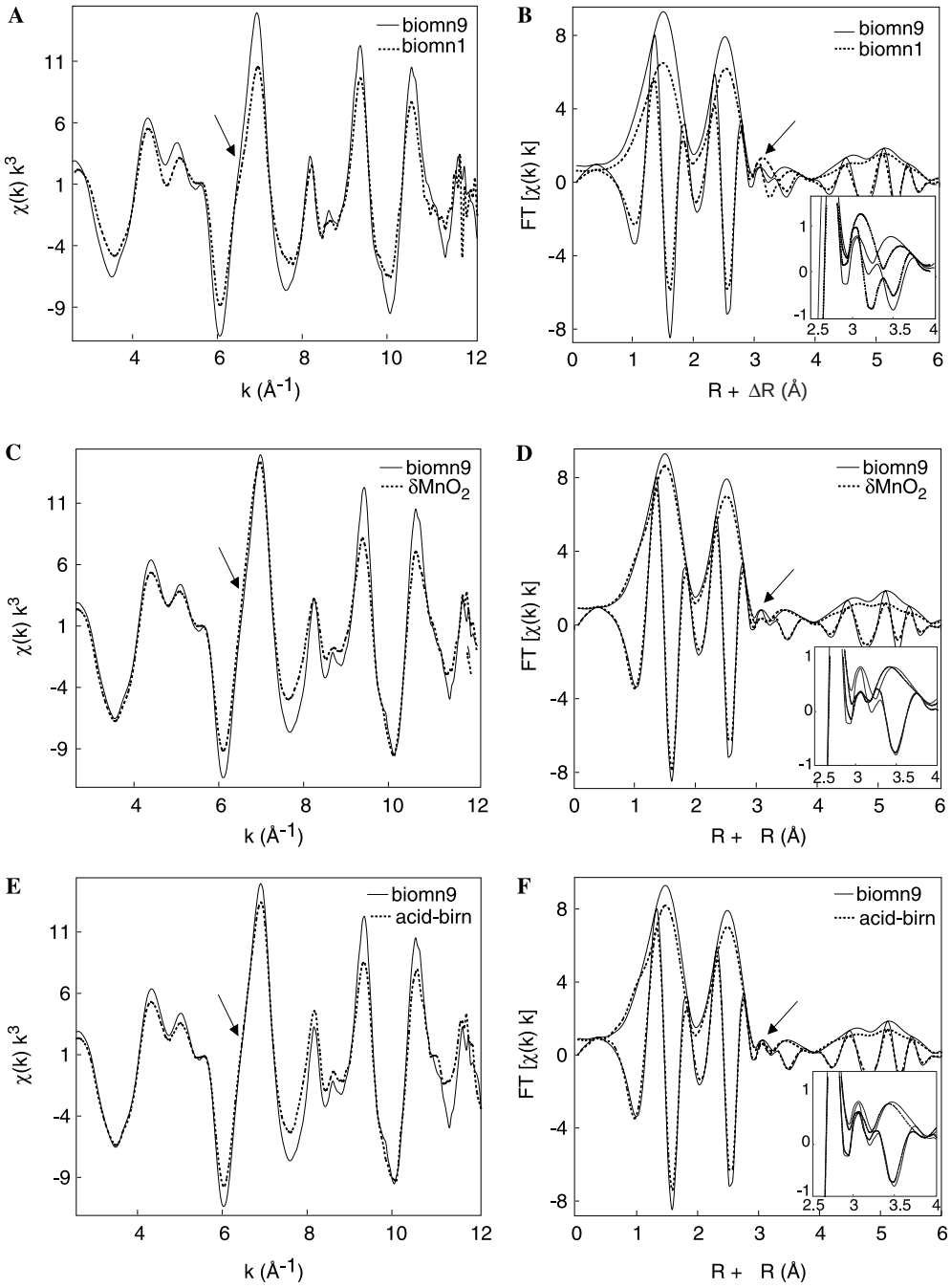

Fig. 10. Manganese EXAFS spectra and FTs of *k*-weighted spectra. The experimental data collected for sample biomn9 is compared to that collected for sample biomn1 (A and B), and reference Mn oxides δMnO_2 (C and D) and acid birnessite (E and F).

atomic neighbors ($N = 4.4 \pm 0.7$) and the Zn–O1 interatomic distance of 1.97 ± 0.01 Å (Table 3). In addition, the second shell Zn–Mn1 interatomic distance (3.36 ± 0.03 Å) is consistent with that reported by Manceau et al. (2002a) for tetrahedral coordination of Zn to hexagonal birnessite (3.35 ± 0.02 Å) at low surface loading (Zn:Mn molar ratio 0.008). Based on the structural similarities between Zn sorbed birnessite at low loading and the biomn1 sample, the local environment of Zn in the biomn1 sample is a tetrahedrally coordinated, tridentate corner-sharing complex with three O atoms of the Mn oxide structure at Mn vacancy positions (Fig. 4).

The results of shell-by-shell and linear least-squares fitting of data collected for sample biomn3 (Zn:Mn molar ratio 0.37) indicate that, in addition to tetrahedrally coordinated Zn, an octahedrally coordinated species is also present. The data for biomn3 were simulated with two Zn–O pairs in the first shell, and two Zn–Mn pairs in the second shell (Table 3). The appearance of an octahedrally coordinated Zn species, in addition to tetrahedral coordi-

Table 5
Selected structural and chemical characteristics of synthetic and biogenic Mn oxides

Name[a]	Formula[b]	Specific surface area $m^2\ g^{-1}$[c]	Average oxid. num.[d]	% Vac.[e]
Acid birnessite	$H_{0.06}K_{0.18}(H_2O)_{0.54}Mn^{III}_{0.08}(H_2O)_{0.24}[Mn^{IV}_{0.88}vac_{0.12}]O_2$	36	3.96	12.0
δMnO_2	$Na_{0.24}(H_2O)_{0.72}[Mn^{IV}_{0.94}vac_{0.06}]O_2$	121	4.02	6.0
Biogenic Mn oxide	$H_aNa_{0.15}(H_2O)_{0.45}Mn^{II,III}_{0.167}(H_2O)_{0.50}[Mn^{IV}_{0.883}vac_{0.167}]O_2$	—	3.90	16.7

[a] The nomenclature and synthesis recipes for acid birnessite and δMnO_2 are reported in Villalobos et al. (2003).
[b] The formula reported for $Mn^{III,IV}$ layer-type Mn oxides are complicated by the high proportions of Mn vacancy sites. Variable "*a*" for biogenic Mn oxide formula depends on whether Mn^{II} or Mn^{III} used to calculate charge balance (Villalobos et al., in press).
[c] N_2 BET surface areas courtesy of Dr. Goldberg, George E. Brown Salinity Laboratory, $\pm 10\ m^2\ g^{-1}$.
[d] The average oxidation number of Mn was determined by chemical titration (±0.02) and by X-ray absorption near edge structure (XANES) spectroscopy (Villalobos et al., 2003).
[e] Refers to the number of structural vacancies in the Mn oxide structure (Villalobos et al., in press).

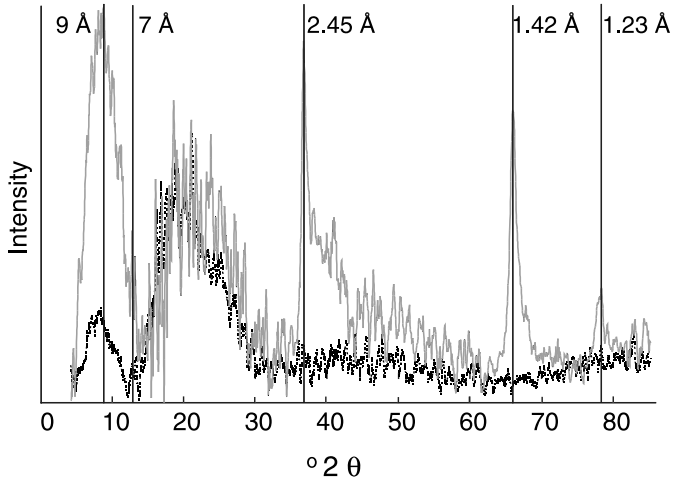

Fig. 11. Synchrotron-radiation X-ray diffraction (SR-XRD) patterns collected for samples of fully hydrated biogenic Mn oxide plus the biofilm (gray line), and biofilm without Mn oxide (black dashed line). The vertical lines indicate the Bragg *d*-spacings associated with the diffraction peaks of the sample and where a 7 Å peak would be located if present.

nation, as Zn loading increases is consistent with a previous study of Zn sorption to birnessite (Manceau et al., 2002a).

Li et al. (2004) reported a study of Zn sorption by synthetic δMnO_2 at pH 5.50 with Zn:Mn molar ratios of 0.03–0.05. Spectral fitting of the EXAFS data produced an average Zn–O1 interatomic distance of 2.07 ± 0.01 Å in the first shell, and Zn–Mn1 at 3.52 ± 0.01 Å in the second shell (Li et al., 2004). Trivedi et al. (2001) also studied Zn sorption by a synthetic hydrous Mn oxide (HMO) at pH 7.0 with Zn:Mn molar ratios of 0.0087–0.87. In that study, the first shell O atoms were fit at a distance of 2.19 Å (error estimates ranging from ±0.01 to 0.07 Å depending on the sample) (Trivedi et al., 2001). The second shell peak was assigned to O with an interatomic distance of 3.46–3.50 Å (Trivedi et al., 2001), this peak assignment is in contrast to the EXAFS results presented here and elsewhere (Manceau et al., 2002a; Li et al., 2004), in which the second peak is denoted as Mn. In the present study, Zn sorption to biogenic Mn oxide was studied at pH 6.9 with Zn:Mn molar ratios of 0.06–0.37. The spectral data in the three studies discussed here, along with those of Manceau et al. (2002a), possess the same features suggesting that Zn speciation within the samples is essentially the same and independent of the experimental conditions used. Li et al. (2004) interpret their EXAFS fit results as Zn in octahedral coordination to O atoms at Mn vacancy sites in a corner-sharing configuration, and therefore, their interpretation is consistent with the results presented here and by Manceau et al. (2002). Inner-sphere metal sorption at Mn vacancy sites of layer Mn oxides has also been observed for Pb and Cu (Manceau et al., 2002a). The presence of a second O shell (Trivedi et al., 2001) in the model rather than a Mn1 shell (present study; Manceau et al., 2002a; Li et al., 2001) leads to a completely different interpretation of Zn sorption to Mn oxide (e.g., outer-sphere complex). Mistakenly identifying a Mn signal for an O signal causes several inconsistencies in the EXAFS results. First, while it is difficult or impossible to detect a second hydration sphere in aqueous Zn samples with EXAFS spectroscopy due to long bond lengths, large degree of disorder in the bonds, and weak scattering power of O atoms, other techniques have measured or predicted the Zn–O interatomic distance produced by the second hydration shell to be 4.20–4.39 Å (Kuzmin et al., 1997). This range of values is not in agreement with second shell Zn–O interatomic distances of 3.46–3.50 Å. Second, a second shell Zn–O assignment is inconsistent with the multiple frequency of the Zn EXAFS data because O atoms (and other low Z elements), in particular those from the second shell in solids, yield a maximum EXAFS amplitude at low *k* values (typically 4–6 $Å^{-1}$) (Manceau and Combes, 1988; Manceau et al., 2000a; Schlegel et al., 2001). In the Zn EXAFS data presented here and elsewhere (Trivedi et al., 2001; Manceau et al., 2002a; Li et al., 2004), multiple frequencies propagate well into the high *k* region of the spectra. We can demonstrate this phenomenon through fitting the spectra collected from chalcophanite and Zn δMnO_2 (pH 7.0 Zn:Mn 0.068) with a second shell of O atoms rather than Mn atoms (Fig. 12). In the second shell Zn–O fits to spectra from both chalcophanite and Zn δMnO_2, the peak amplitude of the simulated wave envelope appeared at lower *k* values than the experimental, degrading the quality of the fit relative to a Zn–Mn1 second shell (Figs. 5A and 6B). The results of these simulations confirm that EXAFS spectroscopy can distinguish between Mn and O atoms in the

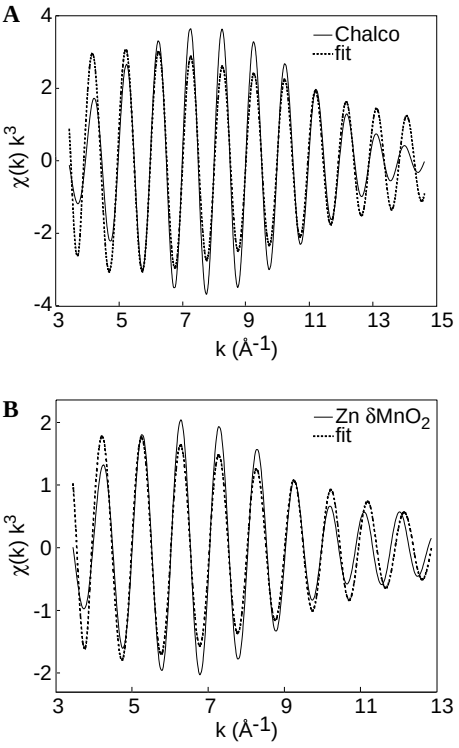

Fig. 12. Simulation of the second shell of chalcophanite (A) and Zn δMnO_2 (B) data with O rather than Mn. The simulated Zn–O wave envelopes (dashed lines) have maximum amplitude at lower k values than the experimental chalcophanite and Zn δMnO_2 data (solid lines). The fit parameters used were (A) chalcophanite: $R = 3.51$ Å, N set to 3.0 based on XRD structure, $\sigma^2 = 0.003$ (Å^2), and $S_0^2 = 2.86$. The physically meaningless value for S_0^2 compensated for the set value of N. (B) The fit parameters for Zn δMnO_2 were, $R = 3.53$ Å, $N = 5.9$, $\sigma^2 = 0.005$ (Å^2), and S_0^2 set to 1.0.

second shell of nearest neighbors, since the structure of chalcophanite is known, and shows that our data are consistent with Mn in the second shell and inner-sphere complexation of Zn at Mn vacancy sites.

Further evidence for Zn sorption at vacancy sites is provided by the Mn EXAFS data. The 6.5 Å^{-1} shoulder observed in the Mn EXAFS spectrum collected for sample biomn1 has been identified in previous studies and indicates the presence of Mn–Mn corner-sharing octahedra (Fig. 10A), i.e., Mn sorbed at vacancy sites in the interlayer of the oxide layer structure (Manceau et al., 1997; Gaillot et al., 2003). In the Mn EXAFS spectra for samples δMnO_2 and acid birnessite, the shoulder at 6.5 Å^{-1} is not visible (Figs. 10C and E). This is consistent with the percentage of interlayer $Mn^{II,III}$ in these samples as determined by XRD: δMnO_2 (0%), acid birnessite (8%), and biogenic Mn oxide (16.7%) (Villalobos et al., in press). In real space, Mn–Mn corner-sharing octahedra yield a third peak at 3.10 Å (Fig. 10B) (Manceau et al., 1997). A comparison of the FTs for samples biomn1 and biomn9 with those of the synthetic Mn oxides confirms that the amount of interlayer Mn at vacancy positions decreased as Zn loading increased; therefore, this is evidence for Zn displacing Mn at these sites. The FT amplitudes of the first peak (Mn–O shell) and second peak (edge-sharing Mn–Mn pairs) increased as Zn loading increased, further suggesting a simplification in the number of local environments for Mn in the sample owing to the disappearance of interlayer Mn.

Principal component analysis of the Zn EXAFS spectral dataset revealed three spectral components. The validity of spectrum biomn1 as a spectral end-member was assessed by removing the spectrum of sample biomn1 from the PCA data set, which confirmed the presence of three remaining components, and conducting target transformation analysis with the spectrum. The SPOIL value for this spectrum was equal to 2.1, indicating that it is a good spectral component for the dataset. Therefore, the spectrum collected from sample biomn1 is a single species end-member (Zn sorbed to Mn oxide in tetrahedral coordination at vacancy sites) and a plausible Zn species present at all Zn loadings examined. Based on the target transformation analysis, the spectrum collected for reference material Zn δMnO_2 was a reasonable spectral component, indicating that octahedrally coordinated Zn species at vacancy sites are also present in the data set. Although the spectrum from chalcophanite represents a single Zn species (octahedral coordination to Mn oxide), and would therefore be the preferred reference for the octahedrally coordinated Zn–Mn biooxide species, the Zn δMnO_2 spectrum gave a better SPOIL value than the chalcophanite (2.3 versus 3.2): this is because the octahedral Zn species is always admixed with tetrahedral Zn in our samples. In other words, the Zn δMnO_2 is a better match for the experimental data because the Zn sorbed species in the Zn δMnO_2 reference have the same spectral properties arising from the same set of interatomic distances as those in the samples (compare Zn–Mn1 for biomn3 and Zn δMnO_2 in Table 3): the values are, 3.35 ± 0.03 and 3.51 ± 0.02 Å for biomn3, 3.39 ± 0.02 and 3.53 ± 0.02 Å for Zn δMnO_2, and 3.49 and 3.50 Å for chalcophanite. The third spectral component is likely an octahedrally coordinated Zn-organic species. This interpretation is based on the target transformation analyses for reference spectra Zn acetate and Zn phytate which indicate both to be good reference spectra for the dataset (Figs. 9D and E); both of these reference materials contain Zn in octahedral coordination to first shell O atoms (fits not shown). A spectrum from an aqueous sample of $ZnNO_3$ however, was a poor reference spectrum for the data set. This result, along with the low concentration of Zn in solution relative to Zn sorbed to biosorbent in the sample pastes, allows us to dismiss entrained solution as the source of the third spectral component of the data set.

The relative contribution to Zn sorption by the biogenic Mn oxide and bioorganic components of the biofilm was examined by linear least-squares fitting of the Zn EXAFS spectra. The best fit to the spectrum from biomn3 was 41 mol% biomn1 and 64 mol% Zn δMnO_2, indicating a combination of tetrahedrally and octahedrally coordinated Zn sorbed solely to the biogenic Mn oxide surfaces. The spectrum from sample biomn4 was best fit with three components, the third modeled by Zn phytate and Zn acetate, with a 5 mol % contribution. As Zn loading increased in

samples biomn5, biomn6, biomn7, and biomn9, the proportion of the Zn organic species increased from ~16–18 to 38 mol% (Table 4).

5. Conclusions

The Mn^{II} oxidizing bacterial culture discussed here presents many possible metal complexing functional groups, both organic and inorganic, to the solution with which it is in contact. In the experiments conducted, we found that Zn speciation evolved as Zn loading to the biosorbent material increased. At the lowest Zn loading (sample biomn1: 0.13 ± 0.04 mol Zn kg^{-1} biosorbent, Zn:Mn molar ratio 0.06), the sorbed Zn species was in tetrahedral coordination to crystallographically well-defined sites, the structural cation vacancies within the biogenic Mn oxide layers. This result indicates that the bioorganic functional groups present in the biofilm did not intervene in Zn sorption by the biogenic Mn oxide. Our results are consistent with those of a study of Pb sorption by hematite and corundum in the presence of a *Burkholderia cepacia* biofilm, wherein reactive sites at the oxide surfaces were not passivated by the biofilm (Templeton et al., 2001).

At an intermediate Zn loading (sample biomn3: 0.72 ± 0.04 mol Zn kg^{-1} biosorbent, 0.37 Zn:Mn molar ratio), an octahedrally coordinated Zn species was detected. Like the tetrahedrally coordinated Zn species, this second species was located at cation vacancy positions. At this intermediate Zn loading, all of the spectroscopically detectable Zn was sorbed by the biogenic Mn oxide. This result is consistent with Zn speciation found in Zn-sorbed birnessite at loadings of 0.069 and 0.128 mol Zn mol^{-1} Mn (Manceau et al., 2002a). As Zn loading increased to 0.88 ± 0.02 mol Zn kg^{-1} biosorbent (sample biomn4), a 5 mol% contribution to Zn sorption by the bioorganic material was estimated. A similar result has been reported for Pb^{II} sorption to aggregates of *Burkholderia cepacia* biofilm and synthetic goethite at pH 6: the oxide component of the aggregates dominates Pb sorption at low Pb loadings, while at intermediate Pb loadings the contribution to sorption by the biomaterial increases (Templeton et al., 2003).

The charge deficiency observed in the biogenic Mn oxide is created by Mn^{IV} vacancy sites, which can be balanced by two Zn^{II} cations, one above and one below each vacancy site (see chalcophanite structure, Fig. 4). The minimum fractional amount of layer Mn vacancies was estimated, from our Zn sorption and EXAFS spectroscopy results, as approximately 0.19 vacancy:Mn (molar ratio); this value is considered a minimum as Mn and other ions such as Ca, Mg, and Na from the growth medium and electrolyte solution may also balance charge. The estimate of the vacancy:Mn molar ratio is in excellent agreement with the ratio obtained through XRD simulation, 0.167 vacancies per octahedral layer sites/0.883 Mn octahedral layer site occupancy = 0.19 vacancy:Mn (Villalobos et al., in press), providing further evidence for a chalcophanite like structure for Zn sorbed to biogenic Mn oxide.

In our study, Zn preferentially partitioned to the biogenic Mn oxide, saturating the layer vacancy sites before Zn sorption to bioorganic material was observed. After layer vacancy site saturation, the bioorganic functional groups present in the biofilm were significant Zn complexing materials. The observed affinity of the bioorganic material for Zn in this study (approximately 0.6 mol Zn kg^{-1}) is in agreement with that observed for *P. putida* biofilms in the absence of Mn oxide (0.64 mol Zn kg^{-1}) (Toner et al., 2005b). The importance of microbial biomass in Zn partitioning in natural waters will likely depend on the presence and amount of Mn oxides, and other high affinity sorbents such as Fe oxides. It follows then, that the results of our study are consistent with those of Zn speciation in mineral soil fractions, where Zn is associated predominantly with inorganic sorbents, such as Mn oxides, even when the origin of those minerals is thought to be biogenic. In addition, the tetrahedrally coordinated Zn birnessite species described here has been identified in soils (Manceau et al., 2000b) and marine ferromanganese nodules (Marcus et al., 2004), and a mixed tetrahedral–octahedral Zn–Mn oxide species has been identified in soil ferromanganese nodules that contain bacteria (Manceau et al., 2003).

Acknowledgments

B.T. and G.S. thank the National Science Foundation Collaborative Research Activities in Environmental Molecular Science (CRAEMS) program for funding (CHE-0089208). We thank Dr. Mario Villalobos (National University of Mexico) for the δMnO_2 sample and the Mn EXAFS spectra for δMnO_2 and acid birnessite. We thank Dr. John Bargar (Stanford Synchrotron Radiation Laboratory, SSRL) for assistance with data collection and interpretation. Portions of this research were carried out at the SSRL, a national user facility operated by Stanford University on behalf of the US Department of Energy (DOE), Office of Basic Energy Sciences. The SSRL Environmental Remediation Science Program is supported by the DOE, Office of Biological and Environmental Research. The SSRL Structural Molecular Biology Program is supported by the DOE, Office of Biological and Environmental Research, and by the National Institutes of Health, National Center for Research Resources, Biomedical Technology Program.

Associate editor: Jeremy B. Fein

References

Bargar, J.R., Tebo, B.M., Bergmann, U., Webb, S.M., Glatzel, P., Chui, V.Q., Villalobos, M., 2005. Biotic and abiotic products of Mn(II) oxidation by spores of the marine *Bacillus* sp. strain SG-1. *Am. Mineral.* **90**, 143–154.

Bargar, J.R., Tebo, B.M., Villinski, J.E., 2000. In situ characterization of Mn(II) oxidation by spores of the marine *Bacillus* sp. strain SG-1. *Geochim. Cosmochim. Acta* **64**, 2775–2778.

Bochatay, L., Persson, P., 2000. Metal ion coordination at the water-manganite (gamma MnOOH) interface II. An EXAFS study of zinc(II). *J. Coll. Interf. Sci.* **229**, 593–599.

Boyanov, M.I., Kelly, S.D., Kemner, K.M., Bunker, B.A., Fein, J.B., Fowle, D.A., 2003. Adsorption of cadmium to *Bacillus subtilis* bacterial cell walls: a pH-dependent X-ray absorption fine structure spectroscopy study. *Geochim. Cosmochim. Acta* **67**, 3299–3311.

Catts, J.G., Langmuir, D., 1986. Adsorption of Cu, Pb and Zn by δMnO_2: applicability of the site binding-surface complexation model. *Appl. Geochem.* **1**, 255–264.

Chan, C., DeStasio, G., Welch, S., Girasole, M., Frazer, B., Nesterova, M., Fakra, S., Banfield, J., 2004. Microbial polysaccharides template assembly of nanocrystal fibers. *Science*, 303.

Fein, J.B., Martin, A.M., Wightman, P.G., 2001. Metal adsorption onto bacterial surfaces: development of a predictive approach. *Geochim. Cosmochim. Acta* **65**, 4267–4273.

Ford, R., Sparks, D., 2000. The nature of Zn precipitates formed in the presence of pyrophyllite. *Environ. Sci. Technol.* **34**, 2479–2483.

Freeman, D.S., Chapman, W.G., 1971. An improved oxalate method for the determination of active oxygen in manganese dioxide. *Analyst* **96**, 865–869.

Fuller, C.C., Harvey, J.W., 2000. Reactive uptake of trace metals in the hyporheic zone of a mining-contaminated stream, Pinal Creek, Arizona. *Environ. Sci. Technol.* **34**, 1150–1155.

Gaillot, A., Flot, D., Drits, V.A., Manceau, A., Burghammer, M., Lanson, B., 2003. Structure of synthetic K-rich birnessite obtained by high-temperature decomposition of $KMnO_4$. I. Two-layer polytype from 800 °C experiment. *Chem. Mater.* **15**, 4666–4678.

Haack, E.A., Warren, L.A., 2003. Biofilm hydrous manganese oxyhydroxides and metal dynamics in acid rock drainage. *Environ. Sci. Technol.* **37**, 4138–4147.

Isaure, M.P., Laboudigue, A., Manceau, A., Sarret, G., Tiffreau, C., Trocellier, P., Lamble, G., Hazemann, J.L., Chateigner, D., 2002. Quantitative Zn speciation in a contaminated dredged sediment by μ-PIXE, μ-SXRF, EXAFS spectroscopy and principal component analysis. *Geochim. Cosmochim. Acta* **66**, 1549–1567.

Kelly, S.D., Boyanov, M.I., Bunker, B.A., Fein, J.B., Fowle, D.A., Yee, N., Kinner, K.M., 2001. XAFS determination of the bacterial cell wall functional groups responsible for complexation of Cd and U as a function of pH. *J. Synchrotron Rad.* **8**, 946–948.

Kelly, S.D., Kemner, K.M., Fein, J.B., Fowle, D.A., Boyanov, M.I., Bunker, B.A., Yee, N., 2002. X-ray absorption fine structure determination of pH-dependent U-bacterial cell wall interactions. *Geochim. Cosmochim. Acta* **66**, 3855–3871.

Kemner, K.M., Kelly, S.D., Lai, G., Maser, J., O'Loughlin, E.J., Sholoto-Douglas, D., Cai, Z., Schneegurt, M.A., Kulpa, C.F., Jrand Nealson, K.H., 2004. Elemental and redox analysis of single bacterial cells by X-ray microbeam analysis. *Science* **306**, 686–687.

Kraemer, S.M., Xu, J., Raymond, K.N., Sposito, G., 2002. Adsorption of Pb(II) and Eu(II) by oxide minerals in the presence of natural and synthetic hydroxamate siderophores. *Environ. Sci. Technol.* **36**, 1287–1291.

Kuzmin, A., Obst, S., Purans, J., 1997. X-ray absorption spectroscopy and molecular dynamics studies of Zn^{2+} hydration in aqueous solutions. *J. Phys. Condens. Matter* **9**, 10065–10078.

Li, X., Pan, G., Qin, Y., Hu, T., Wu, Z., Xie, Y., 2004. EXAFS studies on adsorption-desorption reversibility at manganese oxide–water interfaces II. Reversible adsorption of zinc on δ-MnO_2. *J. Coll. Interf. Sci.* **271**, 35–40.

Madigan, M., Martinko, J., Parker, J., 2000. *Brock Biology of Microorganisms*, ninth ed. Prentice-Hall, Upper Saddle River, NJ.

Malinowski, E.R., 1977. Determination of the number of factors and the experimental error in a data matrix. *Anal. Chem.* **49**, 612–617.

Malinowski, E.R., 1978. Theory of error for target factor analysis with applications to mass spectrometry and nuclear magnetic resonance spectrometry. *Anal. Chim. Acta* **103**, 339–354.

Manceau, A., Combes, J.M., 1988. Structure of Mn and Fe oxides and oxyhydroxides: a topological approach by EXAFS. *Phys. Chem. Minerals* **15**, 283–295.

Manceau, A., Drits, V.A., Silvester, E., Bartoli, C., Lanson, B., 1997. Structural mechanism of Co^{2+} oxidation by the phyllomanganate buserite. *Am. Mineral.* **82**, 1150–1175.

Manceau, A., Lanson, B., Drits, V., 2002a. Structure of heavy metal sorbed birnessite. Part III: results from powder and polarized extended X-ray absorption fine structure spectroscopy. *Geochim. Cosmochim. Acta* **66**, 2639–2663.

Manceau, A., Lanson, B., Drits, V.A., Chateigner, D., Gates, W.P., Wu, J., Huo, D., Stucki, J.W., 2000a. Oxidation–reduction mechanism of iron in dioctahedral smectites: 1. Crystal chemistry of oxidized reference nontronites. *Am. Mineral.* **85**, 133–152.

Manceau, A., Lanson, B., Schlegel, M.L., Harge, J.C., Musso, M., Eybert-Berard, L., Hazemann, J.-L., Chateigner, D., Lamble, G.M., 2000b. Quantitative Zn speciation in smelter-contaminanted soils by EXAFS spectroscopy. *Am. J. Sci.*, 300.

Manceau, A., Marcus, M.A., Tamura, N., 2002b. Quantitative speciation of heavy metals in soils and sediments by synchrotron X-ray techniques. In: Fenter, P.A., Rivers, M.L., Sturchio, N.C., Sutton, S.R. (Eds.), *Applications of Synchrotron Radiation in Low-temperature Geochemistry and Environmental Science*, vol. 49. Mineralogical Society of America, Washington DC, pp. 341–428.

Manceau, A., Tamura, N., Celestre, R.S., Macdowell, A.A., Geoffroy, N., Sposito, G., Padmore, H.A., 2003. Molecular-scale speciation of Zn and Ni in soil ferromanganese nodules from loess soils of the Mississippi Basin. *Environ. Sci. Technol.* **37**, 75–80.

Marcus, M.A., Manceau, A., Kersten, M., 2004. Mn, Fe, Zn and As speciation in a fast-growing ferromanganese marine nodule. *Geochim. Cosmochim. Acta* **68**, 3125–3136.

McKenzie, R.M., 1980. The adsorption of lead and other heavy metals on oxides of manganese and iron. *Austr. J. Soil Res.* **18**, 61–73.

Nelson, Y.M., Lion, L.W., 2003. Formation of biogenic manganese oxides and their influence on the scavenging of toxic trace elements. In: Selim, H.M., Kingery, W.L. (Eds.), *Geochemical and Hydrological Reactivity of Heavy Metals in Soils*. CRC Press, LLC, pp. 169–186.

Newville, M., 2001. IFEFFIT: interactive XAFS analysis and FEFF fitting. *J. Synchrotron Rad.* **8**, 324–332.

Ngwenya, B.T., Sutherland, I.W., Kennedy, L., 2003. Comparison of the acid-base behavior and metal adsorption characteristics of a gram-negative bacterium with other strains. *Appl. Geochem.* **18**, 527–538.

O'Day, P.A., Rivera Jr., N., Root, R., Carroll, S.A., 2004. X-ray absorption spectroscopic study of Fe reference compounds for the analysis of natural sediments. *Am. Mineral.* **89**, 572–585.

Olivie-Lauquet, G., Gruau, G., Dia, A., Riou, C., Jaffrezic, A., Henin, O., 2001. Release of trace elements in wetlands: role of seasonal variability. *Water Res.* **35**, 943–952.

Post, J.E., Appleman, D.E., 1988. Chalcophanite, $ZnMn_3O_7$ $3H_2O$: New crystal-structure determinations. *Am. Mineral.* **73**, 1401–1404.

Ravel, B., 2000. EXAFS analysis using FEFF and FEFFIT. A workshop with course materials available on CD-ROM at <http://feff.Phys.washington.edu/ravel/course/>.

Rehr, J.J., Zabinsky, S.I., Albers, R.C., 1992. High-order multiple-scattering calculations of X-ray absorption fine structure. *Phys. Rev. Lett.* **69**, 3397–3400.

Sarret, G., Balesdent, J., Bouziri, L., Garnier, J.-M., Marcus, M.A., Geoffroy, N., Panfili, F., Manceau, A., 2004. Zn speciation in the the organic horizon of a contaminated soil by micro-X-ray fluorscence, micro- and powder-EXAFS spectroscopy, and isotopic dilution. *Environ Sci Technol.* **38**, 2792–2801.

Sarret, G., Manceau, A., Spadini, L., Roux, J.-C., Hazemann, J.-L., Soldo, Y., Eybert-Berard, L., Menthonnex, J.-J., 1998. Structural determination of Zn and Pb binding sites in *Penicillium chrysogenum* cell walls by EXAFS spectroscopy. *Environ. Sci. Technol.* **32**, 1648–1655.

Saunders, J.A., Prichett, M.A., Cook, R.B., 1997. Geochemistry of biogenic pyrite and ferromanganese coatings from a small watershed—a bacterial connection. *Geomicrobiol. J.* **14**, 203–217.

Schlegel, M.L., Manceau, A., Charlet, L., Hazemann, J.-L., 2001. Adsorption mechanisms of Zn on hectorite as a function of time, pH, and ionic strength. *Am. J. Sci.* **30**, 798–830.

Seki, H., Suzuki, A., Mitsueda, S.-I., 1998. Biosorption of heavy metal ions on Rhodobacter sphaeroides and Alcaligenes eutrophus H16. *J. Coll. Interf. Sci.* **197**, 185–190.

Silvester, E., Manceau, A., Drits, V.A., 1997. Structure of synthetic monoclinic Na-rich birnessite and hexagonal birnessite: II. Results from chemical studies and EXAFS spectroscopy. *Am. Mineral.* **82**, 962–978.

Sposito, G., 2004. *The Surface Chemistry of Natural Particles*. Oxford University Press, New York, NY.

Tebo, B.M., Bargar, J.R., Clement, B.G., Dick, G.J., Murray, K.J., Parker, D., Verity, R., Webb, S.M., 2004. Biogenic manganese oxides: properties and mechanisms of formation. *Annu. Rev. Earth Planet. Sci.* **32**, 287–328.

Templeton, A.S., Spormann, A.M., Brown Jr., G.E., 2003. Speciation of Pb(II) sorbed by *Burkholderia cepacia*/goethite composites. *Environ. Sci. Technol.* **37**, 2166–2172.

Templeton, A.S., Trainor, T.P., Traina, S.J., Spormann, A.M., Brown Jr., G.E., 2001. Pb(II) distributions at biofilm-metal oxide interfaces. *Proc. Nat. Acad. Sci.* **98**, 11897–11902.

Teo, B.K., Joy, D.C., 1981. *EXAFS Spectroscopy, Techniques and Applications*. Plenum Press, New York, NY.

Toner, B., Fakra, S., Villalobos, M., Warwick, T., Sposito, G., 2005a. Spatially resolved characterization of biogenic manganese oxide production within the biofilm of *Pseudomonas putida* strain MnB1. *Appl. Environ. Microbiol.* **71**, 1300–1310.

Toner, B., Manceau, A., Marcus, M.A., Millet, D.B., Sposito, G., 2005b. Zn sorption by a bacterial biofilm. *Environ Sci Technol* **39**, 8288–8294.

Trainor, T.P., Brown Jr., G.E., Parks, G.A., 2000. Adsorption and precipitation of aqueous Zn(II) on alumina powders. *J. Coll. Interf. Sci.* **231**, 259–372.

Trivedi, P., Axe, L., Tyson, T., 2001. XAS studies of Ni and Zn sorbed to hydrous manganese oxide. *Environ. Sci. Technol.* **35**, 4515–4521.

Villalobos, M., Lanson, B., Manceau, A., Toner, B., Sposito, G., in press. Structural model for the biogenic Mn oxide produced by *Pseudomonas putida*. *Am. Mineral*.

Villalobos, M., Toner, B., Bargar, J., Sposito, G., 2003. Characterization of the manganese oxide produced by *Pseudomonas putida* strain MnB1. *Geochim. Cosmochim. Acta* **67**, 2649–2662.

Wang, L., Chua, H., Zhou, Q., Wong, P.K., Sin, S.N., Lo, W.L., Yu, P.H., 2003. Role of cell surface components on Cu+2 adsorption by *Pseudomonas putida* 5-x from electroplating effluent. *Water Res.* **37**, 561–568.

Waychunas, G., Fuller, C., Davis, J., 2002. Surface complexation and precipitate geometery for aqueous Zn(II) sorption on ferrihydrite I: X-ray absorption extended fine structure spectroscopy analysis. *Geochim. Cosmochim. Acta* **66**, 1119–1137.

Webb, S.M., 2005. SIXPACK: A graphical user interface for XAS analysis using IFEFFIT. *Physica Scripta* **T115**, 1011–1014.

Webb, S.M., Gaillard, J.-F., Jackson, B.E., Stahl, D.A., 2001. An EXAFS study of zinc coordination in microbial cells. *J. Synchrotron Rad.* **8**, 943–945.

Wilson, A.R., Lion, L.W., Nelson, Y.M., Shuler, M.L., Ghiorse, W.C., 2001. The effects of pH and surface composition on Pb adsorption to natural freshwater biofilms. *Environ. Sci. Technol.* **35**, 3182–3189.

Yee, N., Fein, J., 2001. Cd adsorption onto bacterial surfaces: a universal adsorption edge? *Geochim. Cosmochim. Acta* **65**, 2037–2042.